Materials Science & Engineering A 801 (2021) 140397

Contents lists available at ScienceDirect

Materials Science & Engineering A

journal homepage: http://www.elsevier.com/locate/msea

# The effect of Y and Nd additions on the microstructure and creep behavior of AZ80

Lingbao Ren [a,*], Carl J. Boehlert [b], Gaofeng Quan [c]

[a] Center for Advancing Materials Performance from the Nanoscale, State Key Laboratory for Mechanical Behavior of Materials, Xi'an Jiaotong University, Xi'an, 710049, PR China
[b] Department of Chemical Engineering and Materials Science, Michigan State University, East Lansing, MI, 48824, USA
[c] School of Materials Science and Engineering, Southwest Jiaotong University, Chengdu, 610031, PR China

ARTICLE INFO

*Keywords:*
Mg alloys
Creep
Microalloying
Twin
Rare earth

ABSTRACT

The effect of yttrium (0.2Y wt.%) and yttrium + neodyminum (0.1Y+0.1Nd wt.%) additions on the long-term (>1200 h) tensile creep and microstructural evolution of AZ80 was investigated at temperatures ranging between 100 °C and 150 °C and stresses ranging between 50 MPa and 100 MPa. The alloying resulted in both the formation of Y- and/or Nd containing particles, and lower tensile strengths and elongation-to-failure. The minimum creep rate ($\dot{\varepsilon}_{min}$) increased with increasing applied creep temperature and stress. Y addition resulted in greater creep-resistance compared with that for (Y + Nd) additions. The $\dot{\varepsilon}_{min}$ of AZ80 + 0.2Y was approximately half that of AZ80 at 50 MPa at 150 °C. The apparent creep activation energy for each alloy ranged between 73 and 93 kJ/mol, and pipe-diffusion-assisted dislocation creep was suggested to be the dominant secondary stage creep deformation mechanism. Discontinuous precipitation (DP) occurred during the creep exposure but was impeded by precipitate-containing twins. The DP was less concentrated in the Y and (Y + Nd) containing alloys, which exhibited lower Vickers hardness values than AZ80. Grain boundary and twin boundary cavitation/cracking were prevalent during creep. Minor Y or (Y + Nd) addition, resulted in less oxidation and extended the intermediate-temperature creep life.

## 1. Introduction

Magnesium (Mg) alloys exhibit excellent specific-strength, thereby offering a means for energy savings as lightweight structural materials in vehicles [1]. Some Mg structural components (i.e. the aircraft landing main wheel and automotive powertrain components) are subject to exposure to intermediate-temperature environments (~150 °C), and therefore require enhancement in intermediate-temperature creep resistance [2]. Mg–Al alloys exhibit insufficient creep resistance which is mostly attributed to the softening of the $\beta$-$Mg_{17}Al_{12}$ phase at a intermediate-to-high temperatures [3–5]. Some strategies, including the substitution of thermally-stable intermetallic compounds for the $\beta$ phase [6–8] and inputting solute-segregation-enhanced grain boundaries (GBs) [9], have been attempted to improve the creep resistance. Another strategy involves the addition of rare-earth (RE) elements, however, this is costly and thereby disadvantageous in terms of scale-up [10].

The essence of microalloying is that minor additions (<1 wt%) of critical elements, such as Y, Nd, Ca, influence dislocation motion, GB characteristics, and precipitation kinetics. Trace alloying elements addition to Mg–Al alloys significantly refine the eutectic $\beta$-$Mg_{17}Al_{12}$ phase and change its volume fraction [11–14], and appropriate microalloying can improve the strength by either refining the grain size or stabilizing disperse, fine secondary phases. For example, (Y + Ca) dual microalloying (<0.5 wt%) can effectively increase the AZ80 ignition temperature to about 820 °C resulting from the double-layered structure of CaO + $Y_2O_3$ and MgO + CaO + $Al_2O_3$ on the molten surface [13]. The periodic segregation of Gd or (Nd + Ag) atoms at twin boundaries (TB) [15,16] or Y, Ca segregation at GBs [17,18] generate a significant drag effect on TB or GB motion, and this microalloying-elements-segregation enhanced stability in TBs and GBs resulted in additional annealing strengthening [16] and the suppression of abnormal dynamic recrystallization grain growth during high-speed extrusion. Recently, microalloying has attracted attention due to the improved creep response [19,20]. In particular, Y, (Y + Nd), and (Y + Ca) multi-microalloying exhibits potential to mediate the grain growth and texture evolution of AZ80 alloys [21]. The enhanced creep resistance in microalloyed Mg–Al

* Corresponding author.
*E-mail address:* renlingbao@mail.xjtu.edu.cn (L. Ren).

https://doi.org/10.1016/j.msea.2020.140397
Received 26 April 2020; Received in revised form 11 August 2020; Accepted 13 October 2020
Available online 15 October 2020

alloys can be attributed to the following: (i) Microalloying elements impede dislocation motion. For example, minor Y additions can reduce the $I_1$ stacking fault energy on basal planes, making <c+a> slip easier to activate [22,23]. (ii) Microalloying elements tend to segregate at interfaces (GB or interphase boundaries) and thereby affect the $\beta$ precipitation kinetics. 0.2–0.8 wt% Y additions to Mg dramatically suppress the static discontinuous precipitation (DP) at GBs [24]. Miao et al. [25] and Liu et al. [26] reported that trace Ag or Zn addition resulted in Ag or Zn segregation at the $\alpha/\beta$ interface, which refined the $\beta$ continuous precipitation and enhanced the aging hardening. Thus, the $\beta$ precipitate volume fraction in Mg–Al varies with microalloying, thereby influencing the creep behavior. (iii) Thermally-stable particles or modified $\beta$ phases can impede the dislocation motion and/or recovery process. Thermally-stable particles, such as $Al_2Y$ and $Al_2Ca$, form in Mg–Al alloys after Y and Ca additions [3,24,27]. First-principles calculations [27] revealed that Ca can effectively improve the structural stability of the $\beta$ phase in Mg–Al alloys. As a result, Ca improves the creep resistance of Mg–Al alloys by reducing the softening effect of the $\beta$ phase. 0.3 wt% Mn addition in Mg–4Al–3La (wt.%) resulted in nanoscale Al–Mn precipitates during 175 °C/75 MPa creep, which reduced the secondary state creep rate by three orders of magnitude [28].

In this work, the effect of small concentrations (<0.2 wt%) of Y and Y + Nd on the creep behavior of AZ80 (Mg–8Al-0.5Zn-0.2Mn, wt.%) was investigated using long-term (>1200 h) tension creep testing at 100–150 °C/50–100 MPa. The creep properties, microstructure evolution, and deformation behavior are discussed.

## 2. Materials and experimental procedures

### 2.1. Materials and processing

The nominal and measured (using inductively coupled plasma mass spectrometer) chemical compositions of the alloys are provided in Table 1. The cast ingots were prepared by resistance melting pure Mg (99.9 wt%), pure Al (99.9 wt%), pure Zn (99.9 wt%), Mg–30Y (wt.%), and Mg-30Nd (wt.%) master alloys, and all the master alloys were preheated at 200–300 °C for 0.5 h then added into the pure Mg and Al melt. The molten Mg was protected from oxidation by a covering flux and $CO_2$+2 vol% $SF_6$ mixed gas. The melt was stirred at 760 °C with refine agent (JMDJ) addition to remove the impurities and homogeneous distribution of alloying elements, then it was held at 740 °C for 50–60 min in a Φ156 mm × 200 mm mild-steel crucible, then poured into a Φ95 mm × 200 mm steel mold which was preheated at 200 °C, and finally it was air cooled. Creep test specimens were cut from the cast billets using electrical discharge machining. Both the tensile and creep specimens had a 50.8 mm gage length and 12.4 mm × 1.8 mm cross section (see in Fig. 1).

### 2.2. Annealing heat treatments

400 °C/4 h annealing treatments were conducted on samples sealed in a quartz glass tube before performing the creep experiments. Prior to performing the heat treatment, the samples were first ground using silicon carbide (SiC) papers through 400, 800, and 1200 grits to remove the surface oxidation and contaminants, followed by ultrasonic bath cleaning with ethanol. The sealed quartz glass tube was placed in a tube furnace and heated to 400 °C, then held for 4 h. The glass tube was evacuated using a mechanical pump for about 10 min before heating to minimize oxidation during the annealing treatment. A thermocouple was spot welded onto the samples to monitor their temperature during the heat treatment. The glass tube was taken out from the furnace, and the sample was cooled to less than 50 °C using compressed air. All annealed specimens were then ground using 1200 grit SiC papers to remove any surface oxidation layer that formed during the heat treatment.

**Table 1**
Chemical compositions of the studied alloys (wt.%).

| Alloy | | Al | Zn | Mn | Y | Nd | Mg |
|---|---|---|---|---|---|---|---|
| AZ80 | Nominal | 8.00 | 0.50 | 0.20 | – | – | Bal. |
| | ICP-MS | 8.34 | 0.42 | 0.15 | – | – | Bal. |
| AZ80 + 0.2Y | Nominal | 8.00 | 0.50 | 0.20 | 0.20 | – | Bal. |
| | ICP-MS | 7.72 | 0.53 | 0.22 | 0.24 | – | Bal. |
| AZ80 + 0.1Y+0.1Nd | Nominal | 8.00 | 0.50 | 0.20 | 0.10 | 0.10 | Bal. |
| | ICP-MS | 7.51 | 0.45 | 0.18 | 0.11 | 0.16 | Bal. |

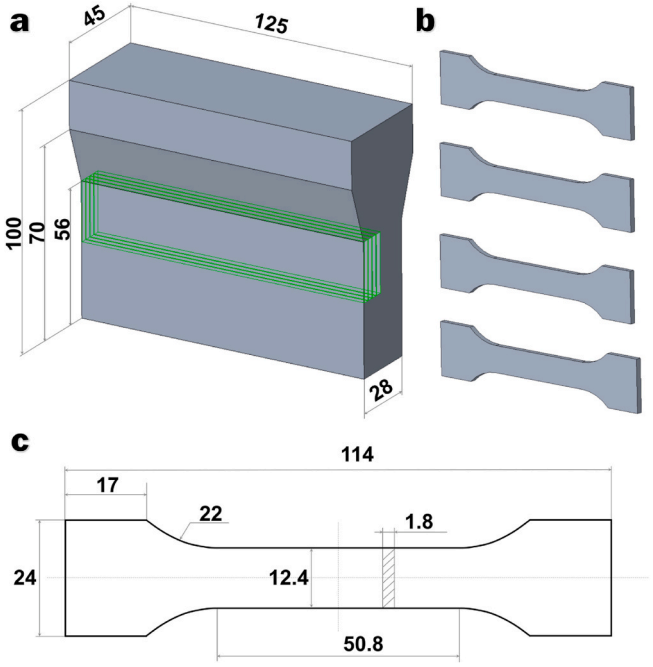


**Fig. 1.** Drawings of the (a) cast billets, and (b) the creep specimens, which were electric discharge machined form the middle of the billet, and (c) the dimensions of the specimen. All dimensions are in mm.

### 2.3. Mechanical properties and creep test

Room-temperature (RT) uniaxial tension tests were performed on the annealed samples using an MTS-CMT5105 universal tensile testing machine. A constant crosshead displacement rate (3 mm/min), corresponding to an initial strain rate of $10^{-3}$ $s^{-1}$, was maintained during the tension tests and the strain was measured using the change of gage length. Three repeat tests for each alloy were performed and the tensile strength and elongation-to-failure ($\varepsilon_f$) values were averaged. Creep tests were performed using Applied Test Systems Incorporated (Butler, PA) lever-arm creep machines, having a 20:1 load ratio, in air at temperatures ranging between 100 and 150 °C. Srinivasan et al. [20] indicated that the critical duration for the transition from the primary stage to the secondary creep stage exceeded 1000 h for intermediate-temperature tension creep of AZ91. Thus, all creep tests in this study lasted longer than 1000 h. Stress-jump tests from 50 to 75 MPa, then to 100 MPa were performed at 100 °C, 125 °C and 150 °C after at least 1000 h of creep. The creep strain was continuously measured throughout the test using a linear variable differential transformer. A three-zone split furnace and a current proportioning temperature controller were used to maintain the test temperature to within ±1 °C. The specimen temperature was measured by spot welding chromel-alume1 thermocouples on one side of the gage section.

### 2.4. Microstructure characterization and hardness test

Metallographic samples were ground using SiC planar grinding papers through 400, 800, 1200 grit, respectively. The samples were then polished through 1.0 μm, 0.25 μm diamond pastes, and 0.04 μm colloidal silica solution was used for the final polishing. The samples were etched using a solution containing 60 ml ethanol, 20 ml water, 15 ml acetic acid, and 5 ml nitric acid. The microstructure of the annealed and deformed specimens was observed using a Nikon 120C optical microscope and a TESCAN MIRA III FEG SEM equipped with an energy dispersive spectroscopy (EDS) system. The SEM accelerating voltage used was 30 kV, and the working distance was 16 mm. The average grain size was estimated by the line intercept method (GB/T 6394–2017) and the phase volume percents were measured by the grid point method. The EDAX-TSL electron backscattered diffraction (EBSD) system was used to identify the grain orientation, and data post-processing was performed using EDAX OIM Analysis 7 software. In addition, Vickers hardness tests were conducted using a LECO M-400-G1 microhardness tester with a 500 g load and a 10 s dwell time. 5 indents tests were performed on the mechanically polished gage and grip sections after the creep tests. The reported hardness values were averaged.

## 3. Experimental results

### 3.1. Annealed microstructures and RT tensile properties

The average grain size of the annealed AZ80, AZ80 + 0.2Y and AZ80 + 0.1Y+0.1Nd were 162 ± 27 μm, 358 ± 42 μm, and 207 ± 13 μm, respectively (Fig. 2). GB secondary phases and intragranular particle phases were present in all the microstructures, and the volume percent of these particles was greater in the Y and (Y + Nd) containing alloys. EDS maps (see Fig. 2(d–f)) illustrated the elements present the intragranular particle phases in the three alloys. For AZ80, Al coexisted with Mn in the particles (see P1 position), which is consistent with the $Al_8Mn_5$ phase. Several multielement particles formed in AZ80 + 0.2Y and AZ80 + 0.1Y+0.1Nd. P1–P4 highlight some of the particles present in the

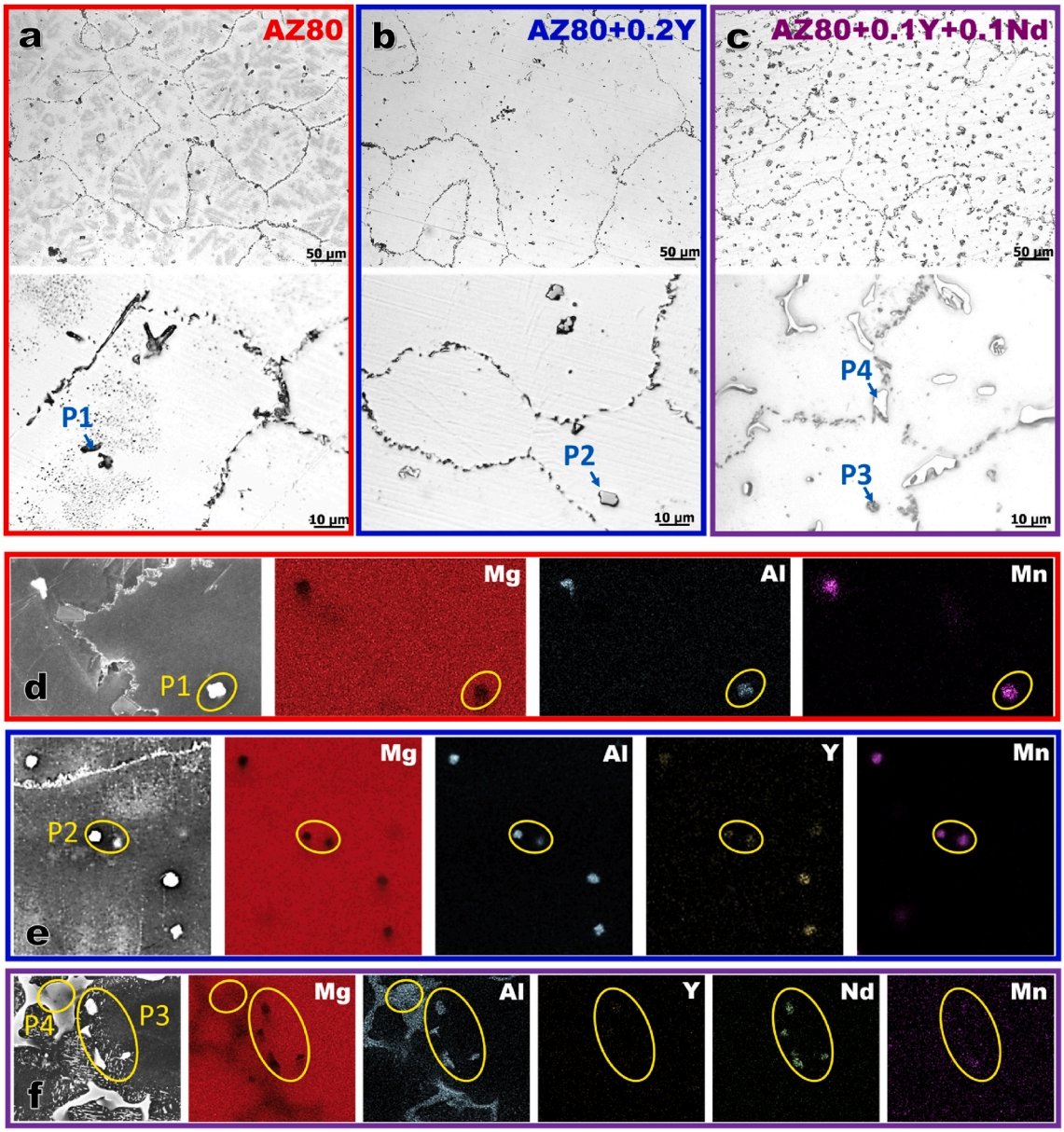


**Fig. 2.** (a–c) Representative optical microscopy images for the annealed AZ80, AZ80 + 0.2Y, and AZ80 + 0.1Y+0.1Nd microstructures, respectively. (d–f) secondary electron SEM (SE−SEM) photomicrographs and EDS maps of some of the particles in AZ80, AZ80 + 0.2Y, and AZ80 + 0.1Y+0.1Nd, respectively.

annealed alloys. For example, Al–Y–Mn- and Al–Y-containing particles were present in AZ80 + 0.2Y, and Al–Y-Nd-Mn-containing particles were present in AZ80 + 0.1Y+0.1Nd (see P3 position).

In addition to the GB secondary phases and the multielement particle phases mentioned above, the $\beta$ divorced-eutectic-phase was also present in the annealed AZ80 + 0.1Y+0.1Nd, see P4 positions in Fig. 2 (c, f). This indicates that the (Y + Nd) addition increases the thermal stability of the $\beta$-$Mg_{17}Al_{12}$ eutectic. A previous report [27] illustrated that the Mg atoms in $Mg_{17}Al_{12}$ can be substituted with Ca solute, which enhances the bonding energy and increases the melting temperature of the $\beta$ eutectic phase. There was no discontinuous precipitation (DP) evident at the GB in these annealed alloys prior to creep testing.

### 3.2. Creep properties

Fig. 3 presents the creep strain versus time ($\varepsilon$-$t$) curves for the annealed alloys. Higher creep temperatures resulted in larger creep strains. The 50 MPa creep stress level was maintained for at least 1000 h. Then 50 → 75→100 MPa stress-jump tests were conducted in all three alloys at 100 °C. Creep failure occurred earlier in the 125 °C/75 → 100 MPa stress-jump tests. The creep rate ($\dot{\varepsilon} = d\varepsilon/dt$) variation with duration (200–1050 h) at 100–150 °C/50 MPa is presented in Fig. 4. The $\dot{\varepsilon}$ continuously decreased with increasing creep time, which indicated that steady-state was not obtained. For example, when the annealed AZ80 creep was tested at 100 °C/50 MPa, $\dot{\varepsilon}$ was $6.1 \times 10^{-10}$ $s^{-1}$ at $t = 200$ h, while $\dot{\varepsilon}$ decreased to $1.5 \times 10^{-10}$ $s^{-1}$ at $t = 1000$ h. In this study, the minimum creep rate, $\dot{\varepsilon}_{min}$, for 50 MPa creep was defined as $\dot{\varepsilon}$ at $t = 1000$ h:

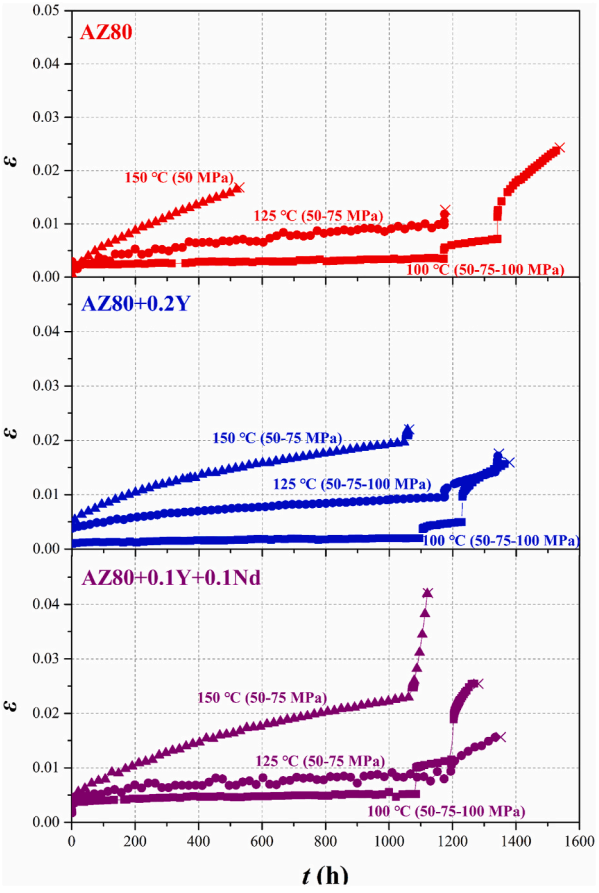


**Fig. 3.** Creep strain, $\varepsilon$, variation with creep time, $t$, for annealed AZ80, AZ80 + 0.2Y, and AZ80 + 0.1Y+0.1Nd at creep temperatures ranging between 100 and 150 °C and stress levels ranging between 50 and 100 MPa.

$$\dot{\varepsilon}_{t=1000h(\sigma=50MPa)} = \dot{\varepsilon}_{min(\sigma=50MPa)} \quad (1)$$

The $\dot{\varepsilon}_{min}$ values at different creep conditions are provided in Table 2. The $\dot{\varepsilon}_{min}$ increased with increasing temperature and stress. Fig. 5 summarizes the $\dot{\varepsilon}_{min}$ variation with Al content in Mg–Al series alloys [29–34]. $\dot{\varepsilon}_{min}$ decreased with increasing Al content. Y addition resulted in greater creep-resistance than that for (Y + Nd), and the $\dot{\varepsilon}_{min}$ of AZ80 + 0.2Y was approximately half that of AZ80 at 150 °C/50 MPa. The histogram in Fig. 6 (a) illustrates the $\dot{\varepsilon}_{min}$ distribution at 100 °C/50–100 MPa for the three alloys. Y addition resulted in a reduction of $\dot{\varepsilon}_{min}$, however, (Y + Nd) additions resulted in a higher $\dot{\varepsilon}_{min}$ than that for AZ80. The difference in $\dot{\varepsilon}_{min}$ between AZ80 and AZ80 + 0.1Y+0.1Nd increased with increasing stress. When tested at 100–150 °C/50 MPa (Fig. 6 (b)), Y addition resulted in the lowest $\dot{\varepsilon}_{min}$, and the AZ80 + 0.1Y+0.1Nd exhibited lower $\dot{\varepsilon}_{min}$ than that of AZ80. Overall, AZ80 + 0.2Y exhibited the greatest creep resistance at 100 °C and a constant stress of 50 MPa. The (Y + Nd) addition increased the thermal stability of the $\beta$-$Mg_{17}Al_{12}$ eutectic, which resulted in a greater volume fraction of the $\beta$ eutectic after the annealing treatment (Fig. 2(c)). The creep resistance of AZ80 + 0.1Y+0.1Nd rapidly degraded with increasing stress (e.g., constant temperature (100 °C) condition). This shows the creep sensitivity of high-$\beta$ vol.%-containing microstructures.

### 3.3. Creep microstructural evolution and vickers hardness

The microstructure near the fracture surface was investigated after the 100–125 °C long-term creep. For the 100 °C creep specimen, see Fig. 7, the DP volume percent for AZ80 and AZ80 + 0.2Y were approximately 9 vol% and 2 vol%, respectively. Twinning occurred in the 100 °C creep test and accommodated the creep deformation. It appeared that the precipitation density within the twins was higher than that within the matrix. Intra-/Intergranular pores were prevalent in AZ80. Most of the intergranular pores preferentially initiated at the triple points and propagated along the GB, see Fig. 7 (a, b). Moreover, it was found that some of the intragranular pores initiated at twin-twin boundaries. Fig. 7 (c) illustrates the lamellar $\beta$ precipitates, which emanated from the twin boundaries. Fig. 7(d–f) shows the 100 °C creep microstructure of AZ80 + 0.2Y. The triple points served as crack initiation sites, while bead-like pores were distributed along GBs accompanied with DP, see in Fig. 7 (e, f).

Increasing temperature promoted DP. Fig. 8 presents the microstructure for the three alloys after 125 °C creep, and the DP volume percent for AZ80 and AZ80 + 0.2Y were approximately 17 vol% and 9 vol%, respectively. There was no DP formation in AZ80 + 0.1Y+0.1Nd, but instead, precipitates surrounded the $\beta$ divorced-eutectic. Twinning occurred during the creep deformation in the 125 °C creep test. Triple points served as preferable void initiation sites for AZ80 (see Fig. 8 (d)), while intergranular cracking occurred in AZ80 + 0.2Y. The EBSD images for the 125 °C creep microstructure in AZ80, shown in Fig. 9, illustrated intergranular void formation.

The gage and grip sections underwent long-term intermediate-temperature aging with and without creep deformation, respectively. As a result, the Vickers hardness in these two sections varied with creep temperature and microalloying elements, see in Fig. 10. For the gage section, higher temperatures accelerated DP, and therefore the hardness increased with increasing creep temperature. Grain coarsening in AZ80 + 0.2Y and AZ80 + 0.1Y+0.1Nd decreased the Vickers hardness, which was consistent with the variation in the RT tensile yield strength results. Either Y or Y + Nd additions can suppress DP, which thereby decreases precipitation hardening [24]. As a result, the AZ80 + 0.2Y and AZ80 + 0.1Y+0.1Nd exhibited lower hardness than that of AZ80 after the creep test. It should be noted that the creep failure occurred at approximately $t$ = 400 h for annealed AZ80 at 150 °C/50 MPa. This short creep time contributed to less DP and thereby less hardening.

The hardness variation with temperature was different in the grip

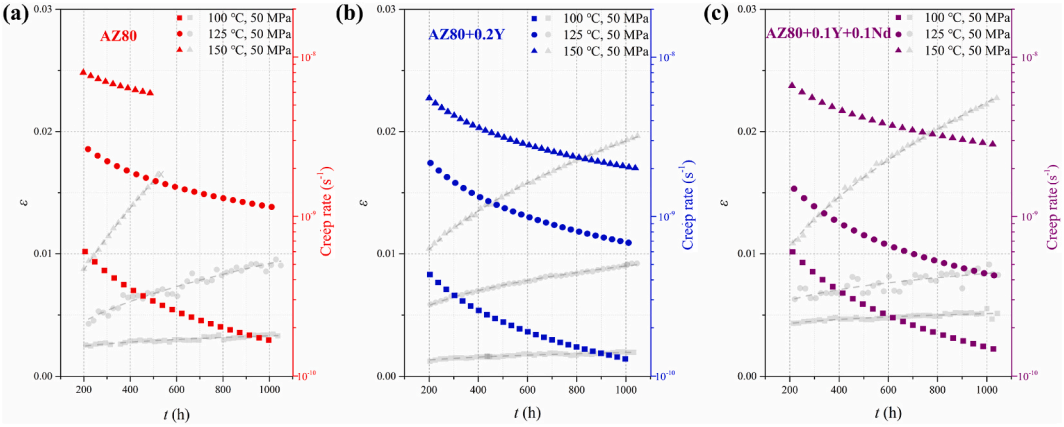


**Fig. 4.** Creep strain, $\varepsilon$, (light grey) and creep rate (colored) variation with creep time for creep conditions including temperatures between 100 and 150 °C at an applied stress of 50 MPa (a) AZ80, (b) AZ80 + 0.2Y, and (c) AZ80 + 0.1Y+0.1Nd.

**Table 2**
Minimum creep rate for the studied alloys at temperatures ranging between 100 and 150 °C and stresses ranging between 50 and 100 MPa.

| Alloy | Stress (MPa) | Minimum creep rate ( $\times 10^{-9}$ $s^{-1}$) | | |
|---|---|---|---|---|
| | | 100 °C | 125 °C | 150 °C |
| AZ80 | 50 | 0.2 | 1.1 | 5.8 |
| | 75 | 2.2 | n.a. | n.a. |
| | 100 | 13.5 | n.a. | n.a. |
| AZ80 + 0.2Y | 50 | 0.1 | 0.7 | 2.1 |
| | 75 | 2.0 | 4.7 | n.a. |
| | 100 | 8.7 | n.a. | n.a. |
| AZ80 + 0.1Y+0.1Nd | 50 | 0.2 | 0.4 | 2.8 |
| | 75 | 3.1 | 10.3 | n.a. |
| | 100 | 23.7 | n.a. | n.a. |

Note: n.a.: not available.

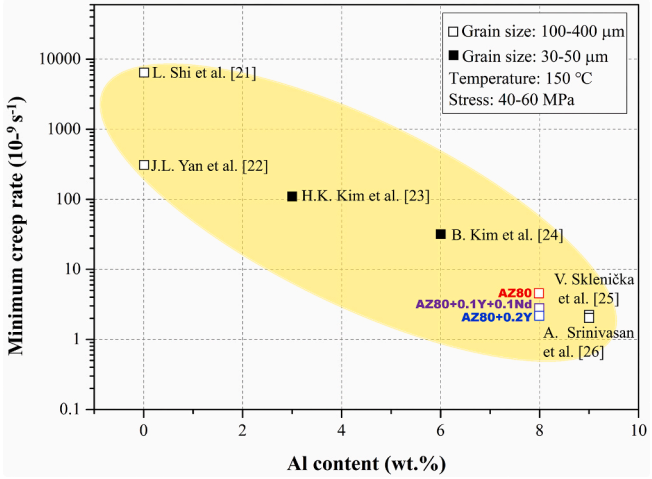


**Fig. 5.** Minimum creep rate versus Al content in Mg–Al series alloys creep tested at 150 °C/40–60 MPa [29–34]. The minimum creep rate of the annealed AZ80, AZ80 + 0.2Y and AZ80 + 0.1Y+0.1Nd at 150 °C/50 MPa studied in this work are also indicated.

and gage sections, where the grip section hardness values were less than those of the gage section for the 100 °C creep tested samples, i.e. the hardness value of AZ80 decreased from 64Hv in the gage to approximately 52Hv in the grip. This was in contrast to that for the 125 °C creep samples, where the grip section exhibited higher hardness than that of the gage section. For example, for AZ80 + 0.2Y, the harness value increased from 70Hv in the gage section to approximately 86Hv in the grip section. For the 150 °C creep tested samples, the hardness of AZ80 + 0.1Y+0.1Nd remained almost the same for the grip and gage sections, while AZ80 and AZ80 + 0.2Y specimens exhibited a hardness reduction of ~20Hv from the grip to the gage section.

### 3.4. Creep fracture

Figs. 11 and 12 show the 125 °C creep fracture surfaces of AZ80 and AZ80 + 0.2Y, respectively. Some of the fracture surface regions exhibited ductile failure characteristics, see the "II" region in Fig. 11. The localized morphology difference exhibited between regions I and II in Fig. 11 suggested that the dominant crack may have initiated at one side of the specimen (near region I), where the long-term intermediate-temperature exposure in air may have caused more oxidation than the other side of the specimen (near region II), where overload fracture and dimples were observed. The high-magnification SE−SEM and BSE-SEM images indicated that some particles remained on the fracture surface, consistent with the microstructural features evident in Fig. 8 (a, d). The equiaxed dimple size was approximately 10 μm in the region II of Fig. 11. As for the creep fracture of AZ80 + 0.2Y, a ductile failure occurred, see region I in Fig. 12. However, brittle fracture features were evident in region II, which was consistent with the GB cracking features in Fig. 8 (e). In addition, there were particles present in region II in Fig. 12.

## 4. Discussion

### 4.1. Creep deformation mechanisms

A phenomenological relationship between the steady-state creep rate ($\dot{\varepsilon}_{\mathbf{min}}$ in this work), and stress, $\sigma$, has been described for steady-state power-law creep [35]:

$$\dot{\varepsilon}_{\min} = A_1 \exp(-Q/kT)(\sigma/E)^n \quad (2)$$

where $A_1$ is a constant, $k$ *is* Boltzmann's constant, $T$ is the absolute temperature. Eq. (2) can also be expressed by:

$$\dot{\varepsilon}_{\min} = A_2 D(\sigma/E)^n \quad (3)$$

where:

$$D = D_0 \exp(-Q/kT) \quad (4)$$

Many investigators have modified Eq. (3) by introducing constants [36]:

$$\dot{\varepsilon}_{\min} = A_2 (DGb/kT)(\sigma/G)^n \quad (5)$$

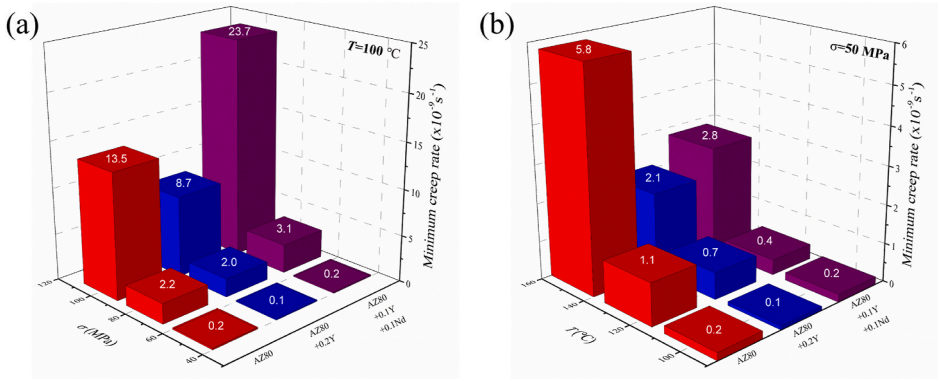


**Fig. 6.** Minimum creep rate comparisons between annealed AZ80, AZ80 + 0.2Y, and AZ80 + 0.1Y+0.1Nd alloys at (a) a creep temperature of 100 °C, and (b) an applied creep stress of 50 MPa.

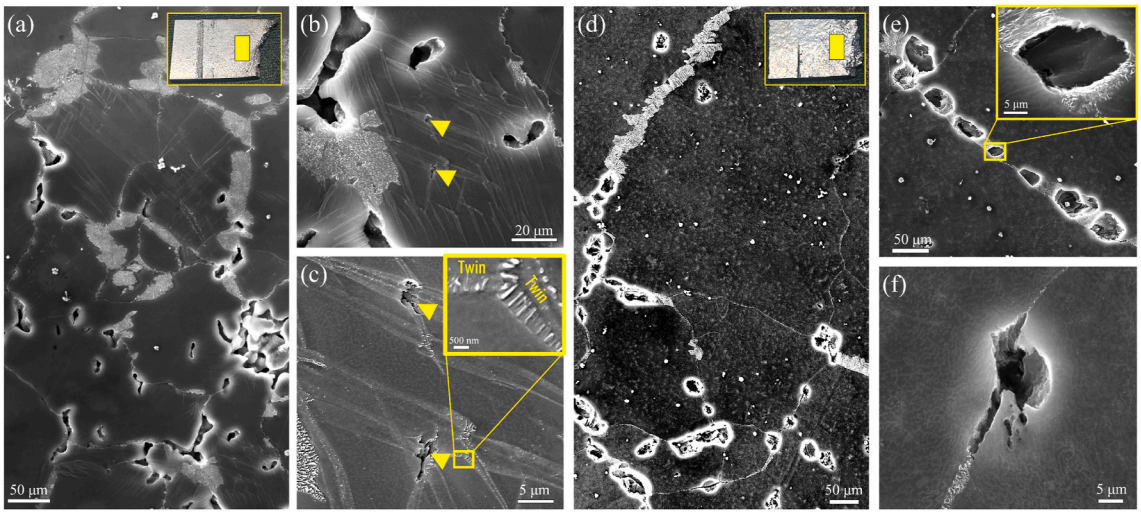


**Fig. 7.** SE−SEM photomicrographs taken of the gage section near the fracture surface after 100 °C creep for (a–c) AZ80, where the $\varepsilon_f$ was 0.25 after a 50 MPa→75 MPa→100 MPa stress-jump test. (d–f) AZ80 + 0.2Y, where the $\varepsilon_f$ was 0.16 after a 50 MPa→75 MPa→100 MPa stress-jump test. The SEM observation positions with respect to the fractured surface are shown in the inserted images in (a, d). The inserts in (c, e) illustrate the microstructural features near cavities. The tensile direction was horizontal.

where the stress exponent, $n$, and creep activation energy, $Q$, can be calculated by:

$$n = \partial\left[\ln\left(\dot{\varepsilon}_{\min} kT\right)/(\mathrm{DGb})\right]/\partial[\ln(\sigma/G)]_T \tag{6}$$

$$Q = \partial\left(\ln\dot{\varepsilon}_{\min}\right)/\partial(-1/kT) \tag{7}$$

$Q$ values similar to that of lattice self-diffusion, $Q_{sd\ (Mg)}$ (135 kJ/mol), and the $n$ values of about 5 for pure metals (called "five-power-law" behavior) generally are observed until the temperature decreases below roughly 0.6 $T_m$ ($T_m$ is the melting temperature), where power-law breakdown occurs, i.e. the $Q$ begins to significantly decrease below $Q_{sd\ (Mg)}$ and $n$ continuously increases [35].

According to the constitutive creep models above, $n$ and $Q$ can be calculated according to Eqs. (6) and (7). Fig. 13 illustrates that the $n$-values for AZ80, AZ80 + 0.2Y, and AZ80 + 0.1Y+0.1Nd were 6.3, 6.1, and 7.3, respectively, and the $Q$-values were 93 kJ/mol, 73 kJ/mol, and 76 kJ/mol, respectively. This suggests that the alloys could be considered to lie within the power-law breakdown creep regime The $Q$ values, which were similar to the activation energy for vacancy diffusion through dislocation pipes, were lower than $Q_{sd\ (Mg)}$ [37]. It was suggested that the rate-controlling mechanism for steady-state creep in the power-law breakdown regime is still dislocation climb, but is facilitated by short-circuit diffusion of vacancies via the elevated density of dislocations associated with increased stress between 0.3 and 0.6 $T_m$ [35]. Fig. 14 shows nano precipitates oriented along dislocation slip traces in adjacent grains (see the yellow dotted line). The kinking trace for the precipitate's distribution in Fig. 14 (b) suggests that cross-slip may be also involved in the creep deformation. The occurrence of nano-bead-like precipitates along the dislocation slip traces in Fig. 14 (a) is consistent with a dislocation dominated creep deformation mechanism.

### 4.2. Creep cracking and oxidation

GBs and the interface between the $\alpha$-Mg matrix and secondary phases are common crack nucleation sites [35]. In the present work, GB cavities preferentially formed at triple points, see Figs. 7–9. Twin boundaries (TBs) are also preferential crack nucleation sites due to the associated shear localization and stress concentrations [38]. TB precipitates have a hardening effect on the TB migration [39,40]. During the intermediate-temperature creep deformation, the lamellar plate-like precipitates that formed near the TB (Fig. 7 (c)) were expected to reduce the TB migration rate, which degrades the twinning accommodation contribution to the local plastic strain. As a result, irregular-shaped cavities tended to nucleate at the twin-twin

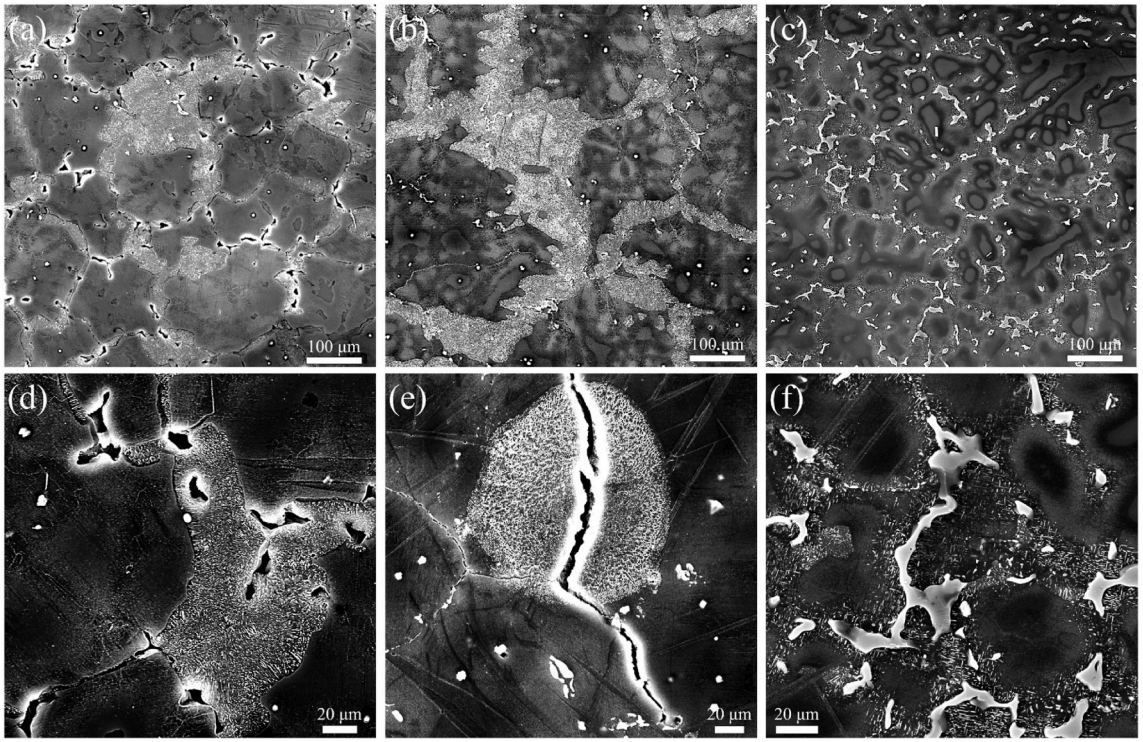


**Fig. 8.** SE−SEM photomicrographs taken of the gage section near the fracture surface after a 125 °C/50 MPa→75 MPa stress-jump test for (a, d) AZ80, (b, e) AZ80 + 0.2Y, and (c, f) AZ80 + 0.1Y+0.1Nd, where the corresponding $\varepsilon_f$ values were 0.12, 0.18, 0.25, respectively. The tensile direction was horizontal.

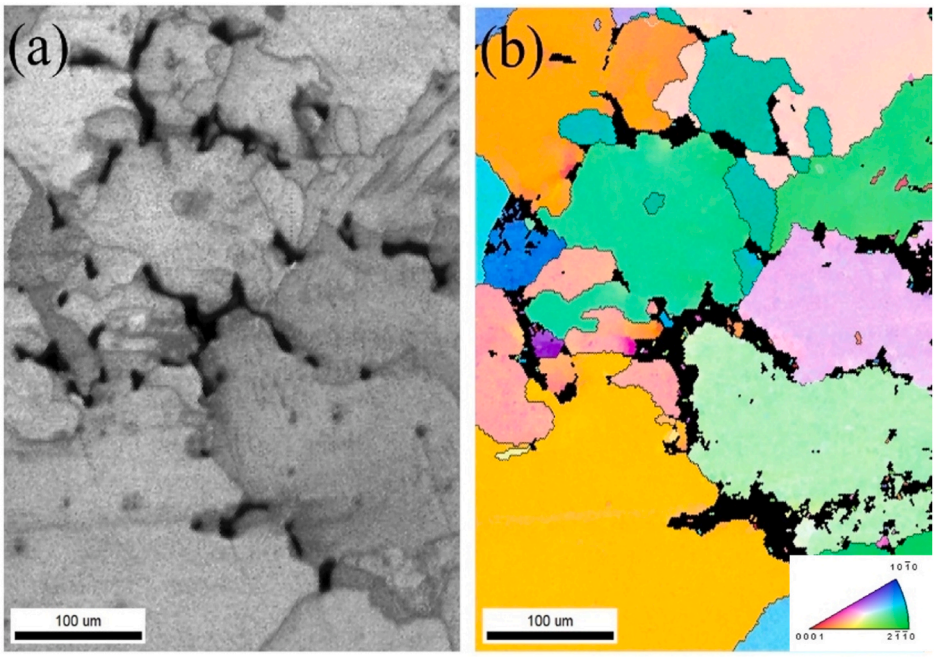


**Fig. 9.** EBSD (a) image quality (IQ) map and (b) inverse pole figure (IPF) taken of the gage section near the fracture surface after a 125 °C/50 MPa→75 MPa stress-jump test for annealed AZ80. The $\varepsilon_f$ was 0.12. The tensile direction was horizontal.

intersections.

Mg exhibits high affinity to oxygen and does not form a dense, slow-growing and protective oxide layer [41]. Thus, degradation of the Mg surface occurs during long-term intermediate-temperature creep in air. Minor additions of rare earth elements with high affinity to oxygen, such as Y, Nd, and Gd, exert a profound effect on the oxidation resistance of Mg alloys [42]. For example, 0.28 wt% was found to be the most effective in suppressing oxidation in AM50 by improving the oxide integrity and its adherence to the substrate [43]. Other research found that an even smaller content (0.1 wt%) of mischmetal caused an improvement in oxidation resistance for Mg alloys [44]. Thus, Y or (Y + Nd) additions are suggested to improve the creep-resistance by hindering the oxidation process of AZ80. Microalloying effects on the oxidation resistance could be manifested as follows: (i) Climb of the misfit

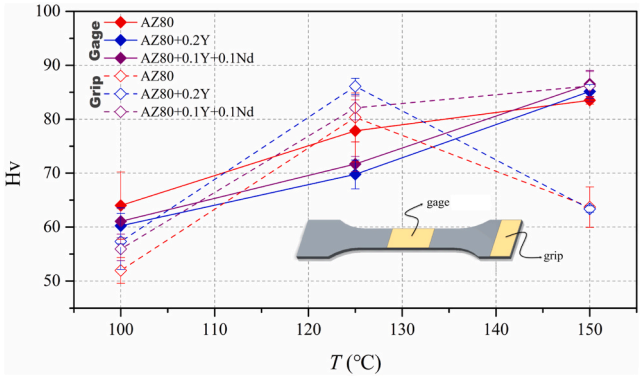


**Fig. 10.** Vickers hardness (Hv) in the gage and grip sections after creep experiments in the temperature range between 100 and 150 °C for annealed AZ80, AZ80 + 0.2Y, and AZ80 + 0.1Y+0.1Nd.

dislocations at the metal-oxide interface can be impeded by the pinning action of the microalloying elements ions, and thereby oxide growth by cation diffusion can be decreased and/or prevented [45]. (ii) Change of the relative magnitudes of cation and anion short-circuit diffusion by the microalloying ions, which segregate to oxide grain boundaries [46]. In the present work, no oxide layer was detected in the AZ80 + 0.2Y. This suggests that minor Y or (Y + Nd) additions may suppress oxidation in AZ80 and thereby extend the creep life.

### 4.3. Twin/DP interactions

Fig. 15 (a) illustrates the DP region in the twin-containing grains in AZ80 + 0.2Y after a 125 °C/50–100 MPa stress jump creep test to a strain of 0.16. The twin interior exhibited denser continuous precipitation than that of the $\alpha$-Mg matrix. The DP front migration was impeded by the twins having larger precipitate densities, see the red square in Fig. 15 (b). The DP front migration is a diffusion-controlled process [47, 48]. Thus, when precipitation preferentially occurs in twins, the Al solute dilution in the front of DP decreases the solute supply thereby affecting the GB diffusion. As a result, the driving force for DP decreases leading to a hindering effect on DP front motion. The hindered effect of twin-preferred precipitation on DP growth is schematically illustrated in Fig. 15 (c). Overall, DP is an important microstructural feature during intermediate-temperature creep. The Y and (Y + Nd) minor additions significantly reduced the DP volume percent consistent with aging results [24]. Moreover, the DP front migration was impeded by twins rich in precipitation. Consequently, the creep resistance is expected to improve based on less $\beta$-$Mg_{17}Al_{12}$ formation.

## 5. Conclusions

Rare-earth microalloying effects on the microstructure and creep deformation behavior of annealed AZ80 were investigated in this work. Based on 1200 h long-term creep and stress-jump tests, the power-law creep model was used to suggest the dominant creep mechanisms. In addition, cavitation nucleation and discontinuous precipitation (DP) were systematically characterized during the intermediate-temperature creep deformation. The following conclusions were offered:

(1) The alloys containing Y and/or Nd exhibited both particles enriched in Y and/or Nd within the grains and at grain boundaries and lower tensile strength and elongation-to-failure compared the baseline AZ80. Minor Nd addition resulted in a considerable amount of the $\beta$ divorced-eutectic phase after annealing, which may be due to the enhanced thermal stability of the $\beta$ phase.

(2) All the alloys examined exhibited continuously decreasing creep rate with increasing creep time and the $\dot{\varepsilon}_{min}$ increased with increasing temperature and load. Y addition resulted in greater creep resistance than the combined addition of (Y + Nd). The $\dot{\varepsilon}_{min}$ of AZ80 + 0.2Y was approximately half that of AZ80 at 50 MPa at 150 °C. Pipe-diffusion-assisted dislocation creep was suggested to be the dominant secondary-stage creep deformation mechanism. The measured activation energies were between 73 and 93 kJ/mol and the $n$-values were approximately 6.1–7.3 for all the tensile-creep conditions evaluated.

(3) Y or (Y + Nd) addition lowered the GB diffusion rate and resulted in less discontinuous precipitation (DP) during the 100–150 °C creep deformation. Increasing the creep temperature promoted diffusion and resulted in more DP near GBs, which was consistent

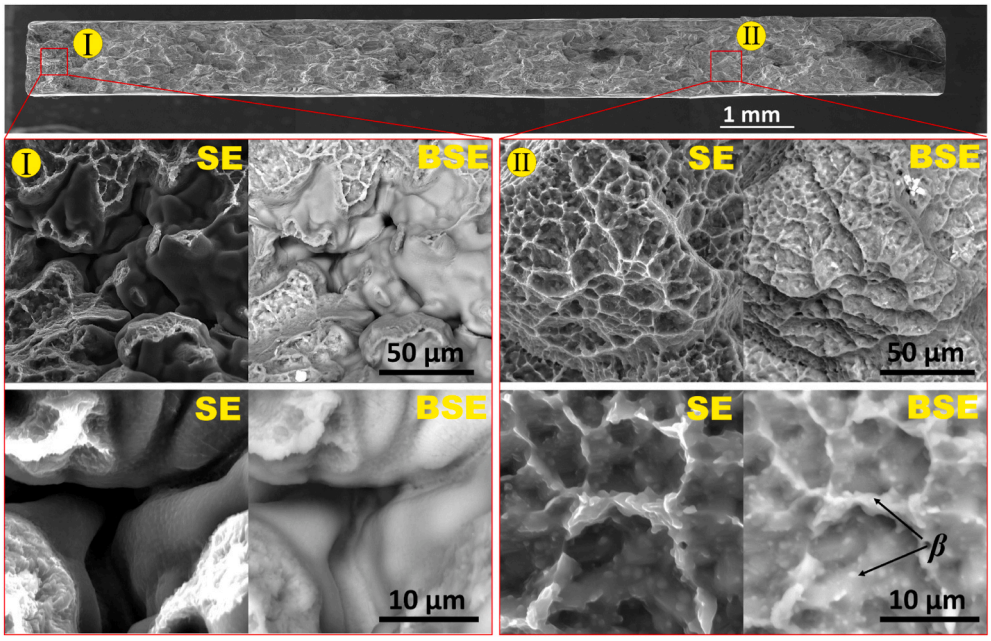


**Fig. 11.** SE - SEM photomicrographs of the fracture surfaces in the crack nucleation region "I" and crack propagation region "II" for annealed AZ80, which underwent a 125 °C/50 MPa→75 MPa stress-jump test. The $\varepsilon_f$ was 0.12.

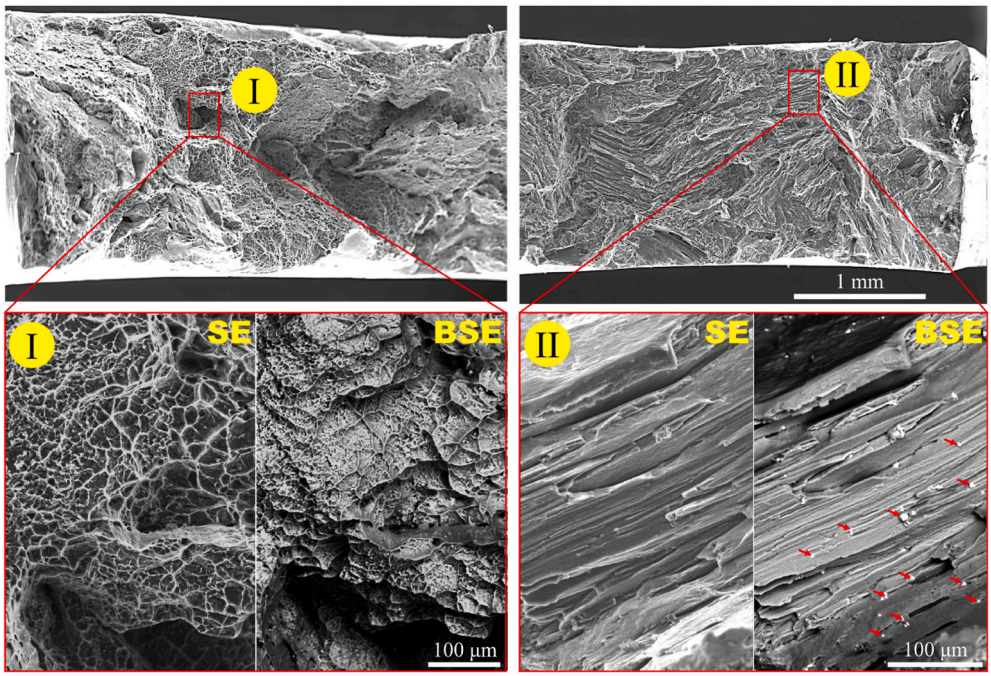


**Fig. 12.** SE–SEM photomicrographs of the fracture surface for annealed AZ80 + 0.2Y, which underwent a 125 °C/50 MPa→75 MPa→100 MPa stress-jump test. The $\varepsilon_f$ was 0.16. The red arrows in "II" region (BSE images) illustrate the Y-containing particles that remained on the fracture surface. (For interpretation of the references to color in this figure legend, the reader is referred to the Web version of this article.)

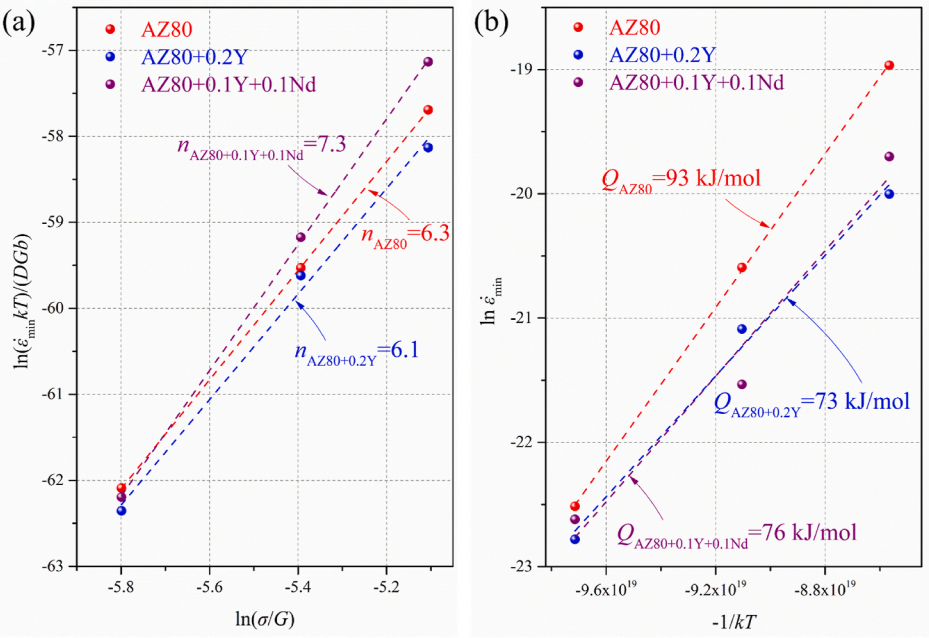


**Fig. 13.** (a) Stress exponent, $n$, and (b) apparent creep activation energy, $Q$, plots for the annealed AZ80, AZ80 + 0.2Y and AZ80 + 0.1Y+0.1Nd during the 100–150 °C/50–100 MPa tensile-creep experiments.

with the Vickers hardness increase with increasing creep temperature. The DP front migration was impeded by the twins rich in precipitates

(4) GB cavitation/cracking was prevalent during creep. Intergranular pores formed in AZ80 during the creep experiments at 100 °C and 125 °C, and GB cracking was prevalent for the alloys containing Y additions. Minor Y or (Y + Nd) addition resulted in less oxidation and extended the intermediate-temperature creep life.

## Author statement

Dr. Lingbao Ren, Experiment design, materials preparation, data processing and discussion, writing, Prof. Gaofeng Quan, Paper reading and discussion, editing; Prof. Carl J Boehlert, Paper reading and discussion, editing and equipment providing.

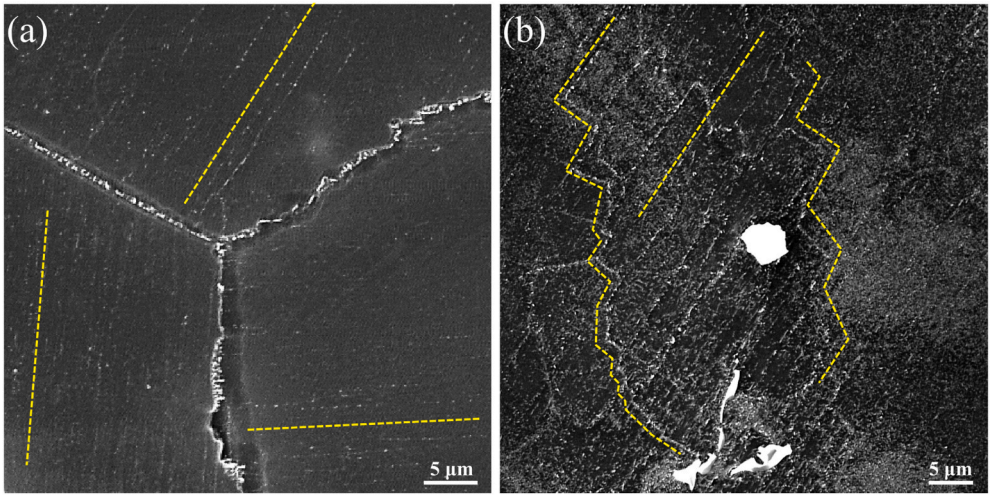


**Fig. 14.** SE−SEM photomicrograph of the nano precipitates along the dislocation slip trace (see for example the yellow dotted lines) during creep. (a) annealed AZ80 after a 100 °C/50 MPa→75 MPa stress-jump test. The $\varepsilon_f$ was 0.12. (b) annealed AZ80 + 0.2Y after a 125 °C/50 MPa→75 MPa stress-jump test creep. The elongation to creep failure was 0.16. (For interpretation of the references to color in this figure legend, the reader is referred to the Web version of this article.)

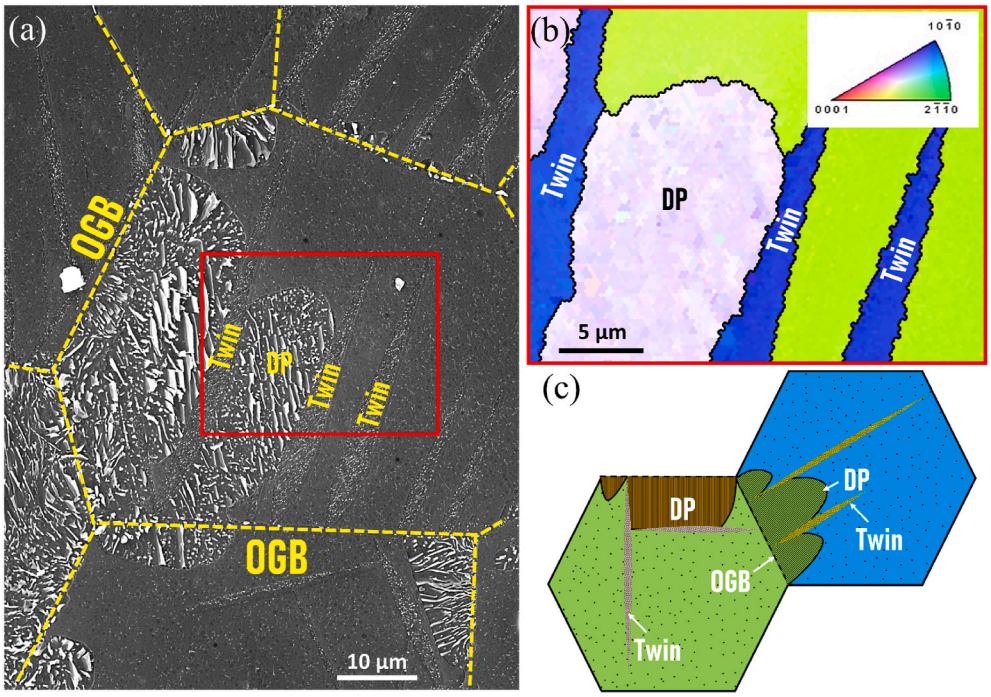


**Fig. 15.** (a) BSE-SEM photomicrograph showing discontinuous precipitation (DP) in annealed AZ80 + 0.2Y after a 125 °C/50–100 MPa stress jump creep test to a strain of 0.16. (b) the corresponding EBSD IPF map corresponding to the highlighted red box in (a). (c) schematic of the twin-DP interaction during intermediate-temperature creep. OGB indicates the original GB position. (For interpretation of the references to color in this figure legend, the reader is referred to the Web version of this article.)

## Declaration of competing interest

The authors declare that they have no known competing financial interests or personal relationships that could have appeared to influence the work reported in this paper.

## Acknowledgments

This work was supported by the National Natural Science Foundation of China (52061040), China Scholarship Council (201707000086) and the financial support from the 2020 open projects (No: KLATM202003) of Key Laboratory of Advanced Technologies of Materials, Ministry of Education China, Southwest Jiaotong University.

Acknowledgments are given to the 2015 Cultivation Program for the Excellent Doctoral Dissertation of Southwest Jiaotong University (received by Lingbao Ren), the Program of the 2015 Doctoral Innovation Fund of Southwest Jiaotong University (received by Lingbao Ren), and the Litmat Technology Chengdu Co., Ltd. The authors also acknowledge the technical support of Dr. Per Askeland and Mr. David Hernández Escobar of Michigan State University.

## References

[1] L.B. Ren, L.L. Fan, M.Y. Zhou, Y.Y. Guo, Y.W.X. Zhang, C.J. Boehlert, G.F. Quan, Magnesium application in railway rolling stocks: a new challenge and opportunity for lightweighting, Int. J. Light. Mater. Manuf. 1 (2) (2018) 81–88.

[2] M. Pekguleryuz, M. Celikin, Creep resistance in magnesium alloys, Int. Mater. Rev. 55 (4) (2010) 197–217.

[3] N. Kashefi, R. Mahmudi, The microstructure and impression creep behavior of cast AZ80 magnesium alloy with yttrium additions, Mater. Des. 39 (2012) 200–210.

[4] J. Ragani, P. Donnadieu, C. Tassin, J.J. Blandin, High-temperature deformation of the γ-Mg17Al12 complex metallic alloy, Scripta Mater. 65 (2011) 253–256.

[5] M. Fukuchi, K. Watanabe, Tensile behavior of γ-phase in Al-Mg system at elevated temperatures, J. Jpn. Inst. Light Metals 30 (1980) 253–257.
[6] B. Nami, H. Razavi, S. Mirdamadi, S.G. Shabestari, S.M. Miresmaeili, Effect of Ca and rare earth elements on impression creep properties of AZ91 magnesium alloy, Metall. Mater. Trans. 41 (2010) 1973–1982.
[7] S.G. Tian, K.Y. Sohn, K.H. Kim, Effect of Sb addition on the creep property of AZ31 alloy, Mater. Sci. Forum 449–452 (2004) 641–644.
[8] F. Czerwinski, A. Zielinska-Lipiec, The microstructure evolution during semi-solid molding of a creep-resistant Mg-5Al-2Sr alloy, Acta Mater. 53 (2005) 3433–3444.
[9] K. Maruyama, M. Suzuki, H. Sato, Creep strength of magnesium-based alloys, Metall. Mater. Trans. 33 (2002) 875–882.
[10] M.A. Bhatia, S.N. Mathaudhu, K.N. Solanki, Atomic-scale investigation of creep behavior in nanocrystalline Mg and Mg-Y alloys, Acta Mater. 99 (2015) 382–391.
[11] Y.B. Hu, C. Zhang, W.Q. Meng, F.S. Pan, J.P. Zhou, Microstructure, mechanical and corrosion properties of Mg-4Al-2Sn-xY-0.4Mn alloys, J. Alloys Compd. 727 (2017) 491–500.
[12] L.B. Ren, M.Y. Zhou, Y.W.X. Zhang, G.F. Quan, C.J. Boehlert, Effect of 0.4 wt.% yttrium addition and heat treatment on the high-temperature compression behavior of cast AZ80, J. Mater. Sci. 54 (2019) 5757–5772.
[13] Y. Go, S.M. Jo, S.H. Park, H.S. Kim, B.S. You, Y.M. Kim, Microstructure and mechanical properties of non-flammable Mg-8Al-0.3Zn-0.1Mn-0.3Ca-0.2Y alloy subjected to low-temperature, low-speed extrusion, J. Alloys Compd. 739 (2018) 69–76.
[14] P. Kumar, A.K. Mondal, S.G. Chowdhury, G. Krishna, A.K. Ray, Influence of additions of Sb and/or Sr on microstructure and tensile creep behaviour of squeeze-cast AZ91D Mg alloy, Mater. Sci. Eng., A 683 (2017) 37–45.
[15] X.J. Zhao, H.W. Chen, N. Wilson, Q. Liu, J.F. Nie, Direct observation and impact of co-segregated atoms in magnesium having multiple alloying elements, Nat. Commun. 10 (2019) 3243.
[16] J.F. Nie, Y.M. Zhu, J.Z. Liu, X.Y. Fang, Periodic segregation of solute atoms in fully coherent twin boundaries, Science 340 (2013) 957–960.
[17] A. Kula, X. Jia, R.K. Mishra, M. Niewczas, Flow stress and work hardening of Mg-Y alloys, Int. J. Plast. 92 (2017) 96–121.
[18] D.A. Basha, H. Somekawa, A. Singh, Crack propagation along grain boundaries and twins in Mg and Mg-0.3 at.%Y alloy during in-situ straining in transmission electron microscope, Scripta Mater. 142 (2018) 50–54.
[19] D. Amberger, P. Eisenlohr, M. Göken, Microstructural evolution during creep of Ca-containing AZ91, Mater. Sci. Eng., A 510–511 (2009) 398–402.
[20] A. Srinivasan, J. Swaminathan, M.K. Gunjan, U.T.S. Pillai, B.C. Pai, Effect of intermetallic phases on the creep behavior of AZ91 magnesium alloy, Mater. Sci. Eng., A 527 (2010) 1395–1403.
[21] L.B. Ren, M.Y. Zhou, C.J. Boehlert, G.F. Quan, Multi-microalloying mediated grain growth and texture evolution during the high-temperature static recrystallization of AZ80 alloys, J. Alloys Compd. 834 (2020) 155077.
[22] K. Hantzsche, J. Bohlen, J. Wendt, K.U. Kainer, S.B. Yi, D. Letzig, Effect of rare earth additions on microstructure and texture development of magnesium alloy sheets, Scripta Mater. 63 (7) (2010) 725–730.
[23] S. Sandlöbes, S. Zaefferer, I. Schestakow, S. Yi, R. Gonzalez-Martinez, On the role of non-basal deformation mechanisms for the ductility of Mg and Mg-Y alloys, Acta Mater. 59 (2) (2011) 429–439.
[24] L.B. Ren, G.F. Quan, M.Y. Zhou, Y.Y. Guo, Z.Z. Jiang, Q. Tang, Effect of Y addition on the aging hardening behavior and precipitation evolution of extruded Mg-Al-Zn alloys, Mater. Sci. Eng., A 690 (2017) 195–207.
[25] J. Miao, W. Sun, A.D. Klarner, A.A. Luo, Interphase boundary segregation of silver and enhanced precipitation of $Mg_{17}Al_{12}$ Phase in a Mg-Al-Sn-Ag alloy, Scripta Mater. 154 (2018) 192–196.
[26] C. Liu, H. Chen, J.F. Nie, Interphase boundary segregation of Zn in Mg-Sn-Zn alloys, Scripta Mater. 123 (2016) 5–8.
[27] D.W. Zhou, P. Peng, H.L. Zhuang, Y.J. Hu, J.S. Liu, First-principle study on the stuctural stability of Ca alloying $Mg_{17}Al_{12}$ phase, Trans. Nonferrous Metals Soc. China 15 (2005) 546–551.
[28] S.M. Zhu, T.B. Abbott, M.A. Gibson, J.F. Nie, M.A. Easton, The influence of minor Mn additions on creep resistance of die-cast Mg-Al-RE alloys, Mater. Sci. Eng., A 682 (2017) 535–541.
[29] L. Shi, D.O. Northwood, Strain-hardening and recovery during the creep of pure polycrystalline magnesium, Acta Metall. Mater. 42 (3) (1994) 871–877.
[30] J.L. Yan, Y.S. Sun, F. Xue, An investigation on the creep behavior of pure Mg, Acta Metall. Sin. 44 (11) (2008) 1354–1359.
[31] H.K. Kim, W.J. Kim, Creep behavior of AZ31 magnesium alloy in low temperature range between 423 K and 473 K, J. Mater. Sci. 42 (15) (2007) 6171–6176.
[32] B. Kim, B. Kang, Y. Park, I. Park, Influence of Pd addition on the creep behavior of AZ61 magnesium alloy, Mater. Sci. Eng., A 528 (18) (2011) 5747–5753.
[33] V. Sklenička, M. Pahutová, K. Kuchařová, M. Svoboda, T.G. Langdon, Creep of reinforced and unreinforced AZ91 magnesium alloy, in: Proceedings of the 1999 8th International Conference on Creep and Fracture of Engineering Materials and Structures 171-174, 2000, pp. 593–600.
[34] A. Srinivasan, K.K. Ajithkumar, J. Swaminathan, U.T.S. Pillai, B.C. Pcampai, Creep behavior of AZ91 magnesium alloy, Procedia Eng 55 (2013) 109–113.
[35] M.E. Kassner, Fundamentals of Creep in Metals and Alloys, third ed., Elsevier, 2015.
[36] A.K. Mukherjee, J.E. Bird, J.E. Dorn, Experimental correlations for high-temperature creep, ASTM Trans. Q. 62 (1969) 155–179.
[37] L.B. Ren, J. Wu, G.F. Quan, Plastic behavior of AZ80 alloy during low strain rate tension at elevated temperature, Mater. Sci. Eng. 612 (2014) 278–286.
[38] M.R. Barnett, Twinning and the ductility of magnesium alloys: Part II. "Contraction" twins, Mater. Sci. Eng., A 464 (1–2) (2007) 8–16.
[39] B.Y. Liu, K.E. Prasad, N. Yang, F. Liu, Z.W. Shan, In-situ quantitative TEM investigation on the dynamic evolution of individual twin boundary in magnesium under cyclic loading, Acta Mater. 179 (2019) 414–423.
[40] H.D. Fan, Y.X. Zhu, J.A. El-Awady, D. Raabe, Precipitation hardening effects on extension twinning in magnesium alloys, Int. J. Plast. 106 (2018) 186–202.
[41] F. Czerwinski, The reactive element effect on high-temperature oxidation of magnesium, Int. Mater. Rev. 60 (5) (2015) 264–296.
[42] M. Abbas, Effect of rare earth oxides ($Y_2O_3$, $Nd_2O_3$) on oxidation kinetics of Al-Li alloys, Nahrain Univ. Coll. Eng. J. 10 (1) (2007) 37–52.
[43] P. Lin, H. Zhou, W. Li, W. li, S. Zhao, J. Su, Effect of yttrium addition on the oxide scale of AM50 magnesium alloy, Corrosion Sci. 51 (2009) 1128–1133.
[44] J. Rao, H. Li, Oxidation and ignition behaviour of a magnesium alloy containing rare earth elements, *Int. J. Adv. Manuf.* Technol. 51 (2010) 225–231.
[45] C. Cotell, G. Yurek, R. Hussey, D. Mitchel, M. Graham, The influence of grain boundary segregation of Y in $Cr_2O_3$ on the oxidation of chromium metal, Oxid. Metals 34 (1990) 173–200.
[46] A. Strawbridge, R. Rapp, The role of reactive elements on scale growth in high-temperature oxidation of pure nickel, iron, cobalt and copper, I: oxidation kinetics and scale morphology, J. Electrochem. Soc. 141 (1994) 1905–1915.
[47] K.N. Braszczyńska-Malik, Discontinuous and continuous precipitation in magnesium-aluminium type alloys, J. Alloys Compd. 477 (1–2) (2009) 870–876.
[48] S.K. Das, N. Brodusch, R. Gauvin, I.H. Jung, Grain boundary diffusion of Al in Mg, Scripta Mater. 80 (2014) 41–44.